

# 3-D Displacement Measurement for Structural Health Monitoring Using Low-Frequency Magnetic Fields

Orfeas Kypris, *Member, IEEE*, and Andrew Markham

**Abstract**—Smart structures of the future will require a cost-effective, easily deployable solution for structural health monitoring. High loads on structures cause stresses that may lead to expansion of gaps, which are of utmost importance when it comes to overall structural health, as they absorb excess stress. Existing methods for direct displacement measurement of expansion joints are not ideal, as they operate under line-of-sight assumptions, are sensitive to moisture, or employ moving parts. In addition, the majority of existing sensors for structural health monitoring are uniaxial, and hence are fundamentally unable to measure 3-D displacement. Importantly, none of the existing wireless sensors for structural health monitoring can be embedded in concrete. We propose a system that uses low-frequency magnetic fields to conduct 3-D displacement measurement directly from within concrete, with a median displacement error of 0.5 mm in all directions, with a maximum separation distance of 50 mm between the transmitter and the receiver. The sensors can be attached to the concrete surface after the building is erected, or can be included in the concrete mix at manufacture, to monitor displacement between gaps in expansion joints, perform crack detection in concrete ties for railroads and in pavements, as well as aid position measurement for the assembly of premanufactured concrete blocks. Embedment in concrete allows operation throughout the lifetime of a structure, providing early warning of impending disaster and helping to inform repair operations.

**Index Terms**—Displacement, magnetic fields, structural health monitoring, crack detection, damage detection, position measurement, concrete.

## NOMENCLATURE

$TX$	Transmitter.
$RX$	Receiver.
$\mathbf{p}$	Position vector from world origin to RX.
$\mathbf{t}$	Position vector from world origin to TX.
$\mathbf{r}$	Position vector from TX to RX.
$\mathbf{b}$	Magnetic flux density vector.
$\mathbf{B}$	Magnetic flux density matrix.
$\mathbf{S}$	Channel matrix.
$\mathbf{m}$	Magnetic moment vector.

Manuscript received August 2, 2016; revised November 9, 2016; accepted November 10, 2016. Date of publication December 23, 2016; date of current version January 19, 2017. This work was supported by EPSRC through the Project entitled Magneto-Inductive Six Degree of Freedom Smart Sensors under Grant EP/M017583/1 (for Structural and Ground Health Monitoring). The associate editor coordinating the review of this paper and approving it for publication was Prof. Subhas C. Mukhopadhyay.

The authors are with the Department of Computer Science, University of Oxford, Oxford OX13QD, U.K. (e-mail: orfeas.kypris@cs.ox.ac.uk; andrew.markham@cs.ox.ac.uk).

Digital Object Identifier 10.1109/JSEN.2016.2636451

$\mathbf{K}$	Calibration matrix.
$\mathbf{k}_{RX}$	RX calibration vector.
$\mathbf{k}_{TX}$	TX calibration vector.
$\mu_{TX}$	Magnetic permeability.
$c$	Model/measurement scaling factor.
$\sigma_{\max}$	Maximal singular value of calibration matrix.
$\langle \mathbb{W} \rangle$	World coordinate frame.
$\langle \mathbb{R} \rangle$	RX coordinate frame.
$\langle \mathbb{T} \rangle$	TX coordinate frame.
$\Theta _{\langle \mathbb{W} \rangle}$	Orientation of TX in the world coordinate frame.
$\Omega _{\langle \mathbb{T} \rangle}$	Orientation of RX in the TX coordinate frame.
$\Omega _{\langle \mathbb{W} \rangle}$	Orientation of RX in the world coordinate frame.
$X_j(t)$	Transmitted voltage sequence from the $j$ th coil.
$Y_i(t)$	Received voltage sequence in the $i$ th coil.
$X_j(\omega)$	Fourier transform of transmitted voltage sequence from the $j$ th coil.
$Y_i(\omega)$	Fourier transform of received voltage sequence in the $i$ th coil.
$S_{ij}(\omega)$	Transfer function.
$\lambda$	Wavelength.
$k$	Wavenumber.
$\delta$	Skin depth.

## I. INTRODUCTION

CIVIL structures such as bridges, railways, and buildings are subject to high and dynamic loads throughout their lifetime. This creates a need for real-time, in-situ monitoring of key structural components in order to warn of impending failure in a timely fashion, as well as inform repair [1], [2]. An important feature present in almost all major civil structures are expansion joints and control joints. Expansion joints, prevalent in bridge decks, are assemblies designed to absorb vibration, high loads, as well as accommodate the expansion and contraction of structural parts due to changes in temperature, and their movement due to landslides, ground settlement and earthquakes. In railroads, expansion joints are necessary to prevent buckling of rail tracks. Control joints in concrete slabs are used to control cracking. Crack formation is also common in precast concrete ties used in railroad tracks, as they are subject to high magnitude loads produced by train wheel abnormalities [3]–[5]. Therefore, direct measurement of displacement within individual blocks of concrete is also a necessary step towards maximizing safety. Displacements and crack widths outside the design tolerance may indicate

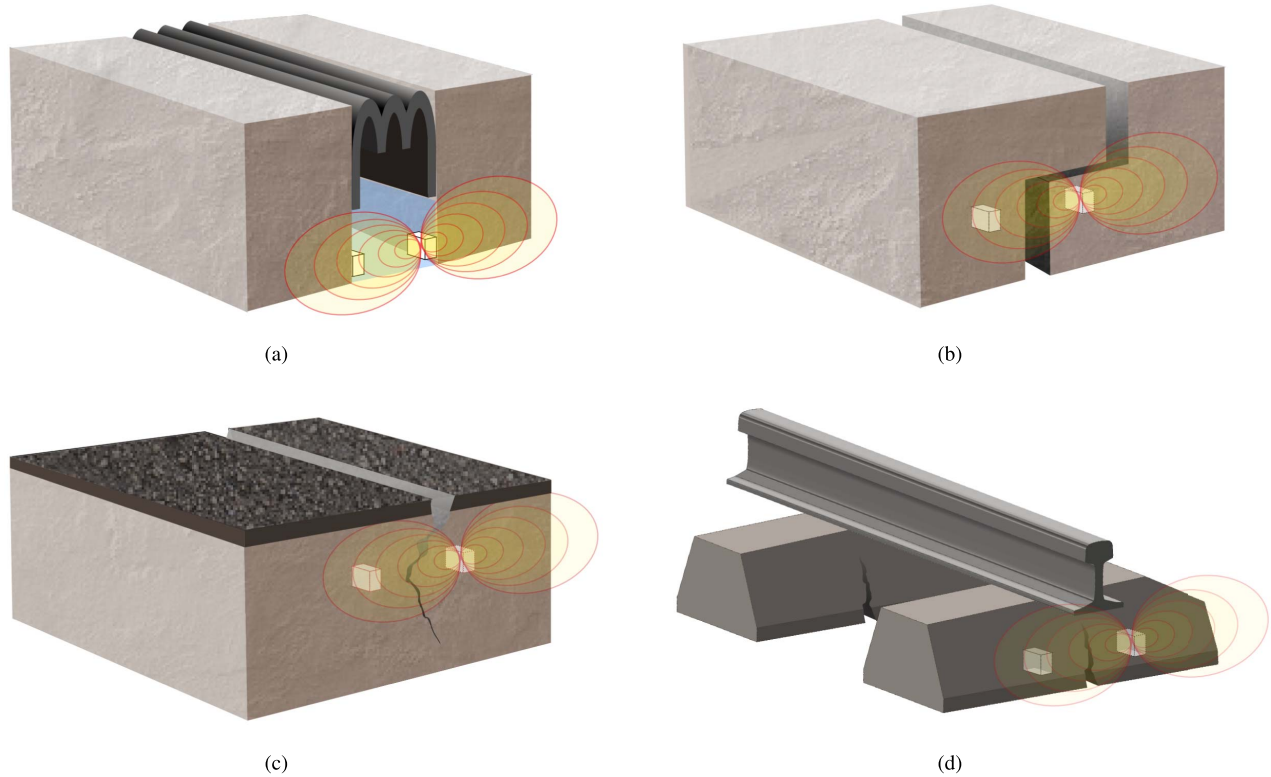


Fig. 1. Four possible use cases, where sensor nodes are: (a) measuring the width of the gap between expansion joints (irrespective of the presence of sealant), (b) embedded in pre-manufactured concrete and measuring their relative position, (c) embedded in concrete and monitoring the width of a crack, and (d) embedded in concrete railroad ties and measuring the width of a crack (graphic of railway track adapted from [63]). Low frequency-magnetic fields, unlike high-frequency electromagnetic waves, are transparent to solid media and can be used to measure 3-D position and orientation.

accumulation of large stress in parts of the structure that cannot withstand it, and in extreme cases this may lead to structural failure and loss of human life. By monitoring the displacement of the adjoint structural components, one can estimate the overall structural health. It has also been shown previously [6] that distributed displacement measurement is a reliable choice for civil structural health monitoring.

One way of estimating gap width in bridge expansion joints is through correlation with ambient temperature [7], [8]. However, this measurement is indirect and thus not ideal, as it is insensitive to random events such as earthquakes. Other indirect methods for monitoring bridge displacement and crack formation include acceleration [9]–[11], vision-based systems [12]–[17], and global positioning systems (GPS) [18]. Acceleration-based systems suffer from accelerometer bias and integration drift for slow-displacements; vision-based systems are costly, and not adequately robust for long-term deployment; differential GPS systems while accurate, are costly to deploy.

Direct displacement monitoring is currently achieved via rotary and linear position sensors that employ movable mechanical parts which experience harsh conditions and are prone to failure. Furthermore, installation after the building is erected is cumbersome. Fiber-optic methods for monitoring displacement [19]–[21] are accurate but expensive to deploy. In order to accommodate large expansions the optical fibres have to be fairly elastic, which is a particular

design challenge. Some commercial solutions [22] employ ultrasonic displacement sensors, which although contactless, operate under line-of-sight assumptions such that their performance is affected by obstructions (such as foam silicone sealant or even debris, which often accumulates in the vicinity of expansion joints) and the elements. Importantly, none of the existing techniques directly measure displacement in three dimensions simultaneously, which is of paramount importance in simultaneously determining static, quasi-static, and dynamic movement of structural components relative to each other and to the ground. Furthermore, acceleration can be calculated from displacement, which can in turn help assess both safety and serviceability [23].

Low-frequency magnetic fields, on the other hand, penetrate most objects (including dielectric materials) and do not suffer from multipath. Such systems have previously been demonstrated in various positioning applications, such as underground animal tracking [24], medical applications [25], [26], as well as sports [27]. We present a low-frequency magnetic 3-D positioning system that employs a pair of rectangular triaxial coils, which can be used as transmitter (TX) and receiver (RX) interchangeably. The sensor nodes can be attached to a concrete surface after the structure has been erected (Fig. 1a). Additionally, since the sensor nodes are embeddable in concrete without any signal attenuation, they can be poured along with the concrete mix at manufacture. This would be particularly suitable for Design for

Manufacture and Assembly (DFMA) for civil infrastructure, and would enable alignment of premanufactured concrete blocks (Fig. 1d).

The proposed system can find a number of application in industry, from process and manufacturing control, to non-destructive evaluation and structural health monitoring of civil structures. Maximum displacements for compression type expansion joints (the most common type) in bridge decks are in the order of 4 inches (102 mm) [28]. In pavements, sealing of cracks is recommended if joint separation or crack width exceeds 1/4 inches (6.4 mm) in the summer or 3/8 inches (9.5 mm) in the winter [29]. Our experimental results show a median overall positioning accuracy below 0.5 mm over a maximum range of 50 mm, whether the sensors are situated in air or embedded in concrete. Thus, the aforementioned length scales make the proposed system very relevant. The specific contributions of the present work are as follows:

- The design of a novel, 3-D displacement sensor that can be directly embedded within dense media such as concrete.
- A technique for optimizing performance of planar COTS rectangular sensing coils which allows for a compact form factor.
- A calibration algorithm which accounts for manufacturing tolerances in the rectangular coils.
- Demonstration of sub-0.5 mm median error in 3-D.

## II. REVIEW OF TECHNOLOGIES FOR DISPLACEMENT MEASUREMENT

For applications where linear displacement occurs, a number of suitable positioning modalities exist, including capacitive, inductive [30], and magneto-inductive systems. Capacitive displacement sensors, which measure the capacitance between the sensor and the target, can achieve resolutions in the order of nanometers and for that reason are used in the semiconductor industry; they work well with conductive and non-conductive targets. However, they are not ideal for structural health monitoring, as capacitance is strongly dependent on moisture content of concrete, which would severely interfere with displacement sensing.

Linear variable differential transformer (LVDT) sensors, which measure the voltage change brought about by the displacement of a magnetic core in the interior of the sensor, are low cost and ideal for use in heavy industrial environments.

Eddy current sensors operate at relatively high frequencies (1 to 5 MHz) [30], and measure the difference in amplitude and phase angle between a primary magnetic field and an induced secondary magnetic field emanating from the target (through measuring changes in inductance in the primary coil). They are generally less expensive than capacitive sensors, not sensitive to material in the gap between the probe and target, and can operate in dirty environments. However, they cannot compete with capacitive sensors in terms of resolution.

Inductive sensors [30] also measure the change in inductance of a primary coil, but due to their lower operation frequency (50 kHz to 1 MHz), are sensitive to the magnetic properties of the target material. Their resolution is typically less than that of eddy-current sensors.

Radio-frequency identification (RFID) technology has also been used for displacement measurement. Previously [31], arrays of radio-frequency identification (RFID) coils were used to measure the length of the gap between two structural elements, in discrete 1" steps. However, due to the high frequency of operation (10's of MHz), the coils could not be embedded in the concrete, but were instead placed on its surface. Furthermore, similar to the aforementioned direct measurement modalities, this system can only measure displacement in one direction. In another study [32] the authors varied the distance between two coupled RFID coils over a 4 mm range, and showed that this altered the center resonant frequency of the system, enabling the measurement of two-dimensional displacement of a movable part w.r.t a fixed part. Even though the authors were able to achieve a good accuracy, the inability to embed the sensor in concrete remains. Furthermore, at RFID frequencies, where the coupling between electric and magnetic field is significant, the signal characteristics are dependent on the relative permittivity of the medium [33], and therefore affected by dielectric materials, such as water; the fact that both distance and moisture content have an impact on the characteristics of RFID signals makes sensor calibration difficult.

Magneto-inductive sensors, which operate at even lower frequencies, and use a permanent magnet as the moving target that attenuates the magnetic field of the sensor coil, work even when the target is obstructed by electrically conducting material, and can achieve accuracy comparable to inductive sensors.

Table I lists industrial sensors belonging to the aforementioned categories along with their characteristics, such as measuring range, resolution and linearity. All of the above systems are relatively bulky, not inherently wireless, and cannot estimate 3-D position.

## III. MEASURING DISPLACEMENT USING LOW-FREQUENCY MAGNETIC FIELDS

Low frequency magnetic-induction based positioning systems use coils to generate and detect magnetic fields in the near-field region [27], [40]–[51]. In a practical sense, the near-field zone occurs when the wavelength of the signal is large compared to the distance between TX and RX (Table II). In this paper, we use three mutually perpendicular coils, both at transmitter (TX) and receiver (RX), which from now on, will be referred to as *triaxial coils*. If the physical channel model (i.e. magnetic field distribution) of the system is known, one can obtain position estimates of the RX w.r.t. TX, by optimizing the model against the measured data and extracting the position vector. A position estimate in  $\mathbb{R}^n$  requires a *single* TX equipped with  $n$  mutually orthogonal coils,  $n \in \{2, 3\}$ . Thus, in 2-D one would only need biaxial units, while in 3-D, triaxial units are required, provided the transmitter is at an edge of the permitted domain; otherwise an ambiguity in the sign of the position vector  $\mathbf{r}$  remains, when both  $\pm \mathbf{r}$  are within the allowable domain. In contrast, range based systems require  $n + 1$  non-colocated transmitters.

TABLE I

LIST OF COMMERCIALY AVAILABLE AND ACADEMIC CONTACTLESS POSITION MEASUREMENT DEVICES, REPRESENTING THE CURRENT STATE OF THE ART IN POSITION MEASUREMENT. IN THIS CONTEXT, THE DEFINITION OF CONTACTLESS MEASUREMENT IS THE ABSENCE OF MECHANICAL WEAR-OUT. MOST OF THE COMMERCIAL DEVICES ARE INTEGRATED IN ONE UNIT AND ONLY ALLOW ONE SIMULTANEOUS DEGREE OF FREEDOM. RESOLUTION AND LINEARITY, ARE DEFINED AS THE SMALLEST DISPLACEMENT THAT CAN BE DETECTED BY THE SENSOR, AND THE MAXIMUM DEVIATION FROM THE THEORETICAL SIGNAL-POSITION CHARACTERISTIC RESPECTIVELY, AND ARE CALCULATED WITH RESPECT TO THE FULL SCALE OUTPUT (FSO) OF THE SENSOR, WHICH IS DEFINED AS THE SIGNAL OUTPUT MEASURED AT THE MAXIMUM DISPLACEMENT FOR WHICH THE SYSTEM IS CALIBRATED. THE OUTPUT OF THIS SYSTEM IS LINEAR, WHICH IS WHY ACCURACY IS QUOTED INSTEAD OF LINEARITY. THE MAIN ADVANTAGE OF THE PROPOSED SYSTEM IS THAT THE COMPACT NODES CAN FORM A SENSOR NETWORK THAT MEASURES POSITION AND STRAIN AT 3 SIMULTANEOUS DEGREES OF FREEDOM (DOF)

Device	Maximum Range	Resolution (w.r.t FSO)	Linearity (w.r.t FSO)	Degrees of Freedom (DOF)
<b>Capacitive</b>				
capaNCDT 6110 (Micro-Epsilon) [34]	10 mm	0.0100%	$\pm 0.05\%$	1-D
Capteura 520 Series System (Capacitec) [35]	2.5 mm	0.0015 %	$\pm 0.05\%$	1-D
<b>Eddy Current</b>				
eddyNCDT 3001 (Micro-Epsilon) [34]	4 mm	0.1000%	$\pm 0.7\%$	1-D
ECL202 (Lion Precision) [36]	15 mm	0.01%	$\pm 0.20\%$	1-D
<b>Inductive</b>				
induSENSOR VIP series (Micro-Epsilon) [34]	150 mm	0.0300%	$\pm 0.25\%$	1-D
BIP 103 (Balluff) [37]	103 mm	0.0800%	0.4000%	1-D
EX-500 series (Keyence) [38]	10 mm	0.0300%	$\pm 0.3\%$	1-D
ECL202 (Lion Precision) [36]	15 mm	0.002% - 0.009%	$\pm 0.20\%$	1-D
<b>Magneto-inductive</b>				
mainSENSOR (Micro-Epsilon) [34]	55 mm	$< 0.05\%$	$< \pm 3\%$	1-D
BIL 60 (Balluff) [37]	60 mm	0.0003%	1.6667%	1-D
<b>RFID</b>				
RFID displacement sensor (M.I.T.) [39]	40 mm	6.2%	Unreported	1-D
RFID displacement sensor (T.U. Darmstadt) [32]	4 mm	6%	Unreported	2-D
<b>Low-frequency magnetic</b>				
This work (University of Oxford)	50 mm	0.5%	3.5% (acc.)	3-D

TABLE II

EQUIVALENT DEFINITIONS OF NEAR-FIELD, TRANSITION ZONE, AND THE FAR-FIELD, USING THREE COMMON MEASURES (WAVELENGTH  $\lambda$ , WAVENUMBER  $|k|$ , AND SKIN DEPTH  $\delta$ ) FOR ELECTROMAGNETICALLY SHORT ANTENNAS

Properties	Near field	Transition zone	Far Field
wavelength	$r \ll \lambda$	$\lambda < r < 2\lambda$	$r \gg 2\lambda$
wavenumber	$ kr  \ll 2\pi$	$2\pi <  kr  < 4\pi$	$ kr  \gg 4\pi$
skin depth	$r \ll 2\pi\delta$	$2\pi\delta < r < 4\pi\delta$	$r \gg 2\pi\delta$

#### A. Magnetic Field in Free Space

When  $r > 3a$ , where  $a$  is the mean radius of the TX coil, it is possible to treat the TX as an infinitesimal (point) magnetic dipole operating in the near field. In free space, the magnetic flux density of the point dipole positioned at the origin of the world coordinate frame (see Appendix VII for a definition of the coordinate system) takes on the following form [52], [53]:

$$\mathbf{b}(\mathbf{r}, \mathbf{m}) = \frac{\mu_{TX}}{4\pi \|\mathbf{r}\|^3} \left( \frac{3\mathbf{r}\mathbf{r}^T}{\|\mathbf{r}\|^2} - \mathbf{I}_3 \right) \mathbf{m} \quad (1)$$

where  $\mathbf{b}(\mathbf{r}, \mathbf{m})$  is the magnetic flux density at the position vector  $\mathbf{r} = [x, y, z]^T$  due to magnetic dipole moment  $\mathbf{m}$ ,  $\mathbf{I}_3$  is the  $3 \times 3$  identity matrix, and  $\mu_{TX}$  is the magnetic permeability of the TX coil. Using (1), it is possible to recover the 3-D position of TX w.r.t RX, from measurements of the 3-D magnetic field vector measured at the RX position, in free space [53].

However, for distances  $r < 3a$ , the model of (1) is invalidated. To accurately represent the magnetic field  $\mathbf{b}(\mathbf{r}, \mathbf{m})$  the finite coil dimensions have to be taken into account. The coils used in the present study are of rectangular cross section; the Biot-Savart law can be readily used to obtain closed-form

analytical expressions to describe the field:

$$\mathbf{b}(\mathbf{r}, \mathbf{m}) = \frac{\mu_{TX}}{4\pi} \int_C \frac{d\mathbf{m} \times \mathbf{r}}{\|\mathbf{r}\|^3} \quad (2)$$

where the infinitesimal magnetic moment  $d\mathbf{m} = I d\mathbf{l}$  (where  $I$  is the current and  $d\mathbf{l}$  is the infinitesimal length element),  $C$  is the integration contour. In the case of a rectangular coil, the integral in (2) can be split up into a sum of 4 contributions, one for each side of the coil [54].

#### B. Channel Model

Each coil on the RX measures one vector component of the field of the TX coil that is currently excited. Since there are three TX coils, there are three excitation vectors,  $\mathbf{e}_1 = [1, 0, 0]^T$ ,  $\mathbf{e}_2 = [0, 1, 0]^T$ , and  $\mathbf{e}_3 = [0, 0, 1]^T$ , representing the coils with magnetic moment oriented in the x-,y-,and z-directions, respectively. This makes the excitation matrix  $[\mathbf{e}_1, \mathbf{e}_2, \mathbf{e}_3]$  equal to  $\mathbf{I}$ .

The measured flux density at the RX position will be:

$$\mathbf{B}|_{\langle \mathbb{T} \rangle} = [\mathbf{b}(\mathbf{r}, \mathbf{e}_1), \mathbf{b}(\mathbf{r}, \mathbf{e}_2), \mathbf{b}(\mathbf{r}, \mathbf{e}_3)] \quad (3)$$

This  $3 \times 3$  matrix is expressed in the TX coordinate frame  $\langle \mathbb{T} \rangle$ , the field is generated at the TX (for a detailed description of coordinate frames see Appendix VII). We can define the  $3 \times 3$  MIMO (multiple-in and multiple-out) channel matrix in the RX frame, by left multiplying  $\mathbf{B}|_{\langle \mathbb{T} \rangle}$  by  $\mathbf{\Omega}|_{\langle \mathbb{T} \rangle}^T$ :

$$\mathbf{S}|_{\langle \mathbb{R} \rangle} = c \mathbf{\Omega}|_{\langle \mathbb{T} \rangle}^T \mathbf{B}|_{\langle \mathbb{T} \rangle} \quad (4)$$

where  $c$  is a range-dependent scaling factor ( $c \propto r^{-2}$  in 2-D and  $c \propto r^{-3}$  in 3-D), which also incorporates the TX/RX coils specific parameters (area, number of turns, amplifier gain) and can be determined by calibration from measurements taken at

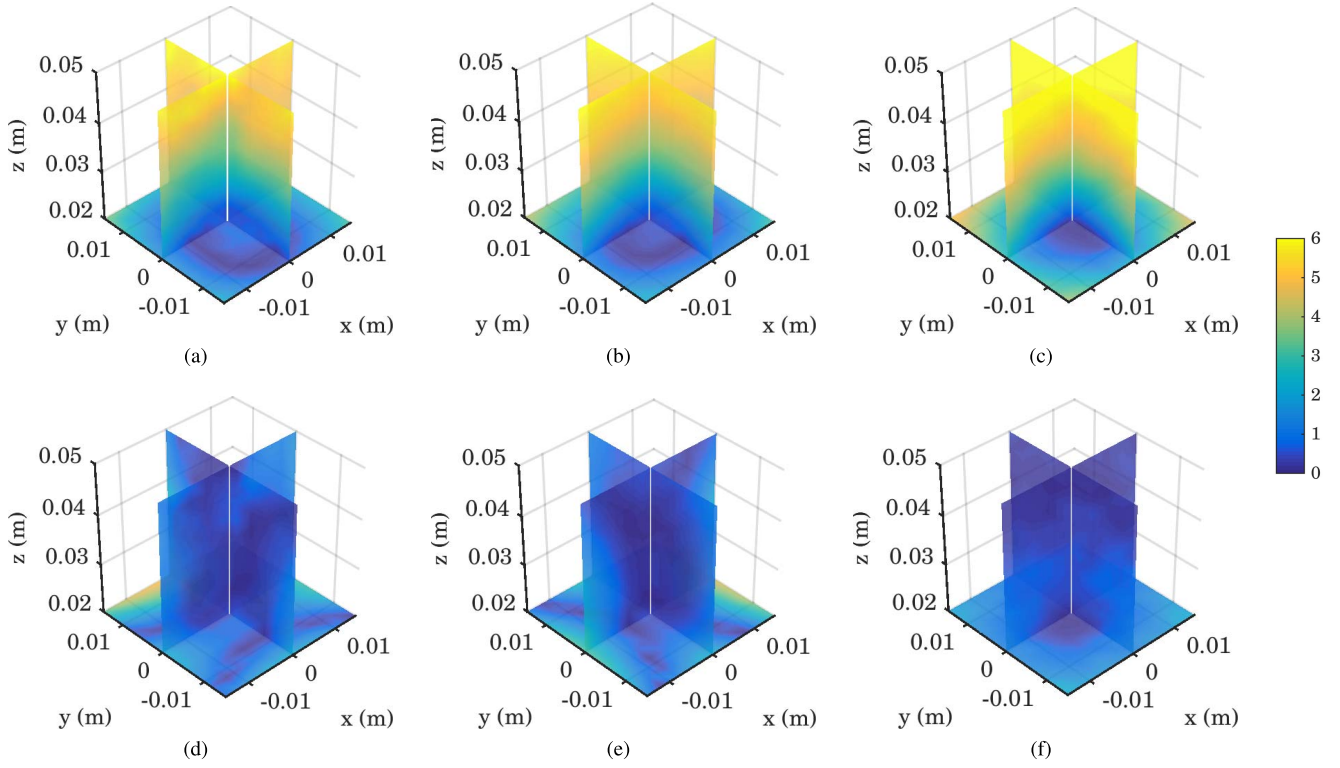


Fig. 2. Norm of the difference in  $\mathbf{b}(\mathbf{r}, \mathbf{m})$ ,  $\|\mathbf{b}_{\text{meas}}(\mathbf{r}, \mathbf{e}_i) - \mathbf{b}_{\text{model}}(\mathbf{r}, \mathbf{e}_i)\|$ , for all transmitter axes ( $\hat{x}$ ,  $\hat{y}$  and  $\hat{z}$  oriented dipoles) between the (a)-(c) dipole model and measurements, (d)-(f) rectangular coil model and measurements. The measured field is best predicted by the rectangular coil model, in all cases. Scale is in dB below maximum value.

known distances [53]. It should be noted that by applying the transformations in (4),  $\mathbf{S}$  is expressed in the RX frame. Furthermore,  $\Theta|_{\langle \mathbb{W} \rangle}$  is contained inside  $\mathbf{B}|_{\langle \mathbb{T} \rangle}$ , and is equal to  $\mathbf{I}$  (since the excitation matrix is also equal to  $\mathbf{I}$ ).

The difference between the performance of the two models (dipole, and rectangular coil model) can be seen in Fig. 2 which shows the error measure  $\|\mathbf{b}_{\text{meas}}(\mathbf{r}, \mathbf{e}_i) - \mathbf{b}_{\text{model}}(\mathbf{r}, \mathbf{e}_i)\|$ , for  $i \in \{1, 2, 3\}$ .

#### IV. EXPERIMENTAL SETUP

##### A. Overview

The system was implemented using the following equipment:

- A pair of Premo [55] 3DC1515 triaxial coils for TX and RX. The TX was embedded in concrete (Fig. 4).
- Three (one for each axis) Zaber T-LSM050A miniature motorized linear slides [56] with a minimum step size of  $0.047625 \mu\text{m}$ . These are used for displacing the RX w.r.t. TX, and also for providing ground truth position.
- A National Instruments 7855-R [57], R-Series Multifunction RIO with Kintex-7 70T FPGA.
- Custom 3D-printed parts for mounting RX and TX.
- A PC equipped with National Instruments LabVIEW [57] and Mathworks MATLAB software [58].

The main steps to acquiring a displacement estimate are as follows:

- 1) An OFDM (Orthogonal Frequency-Division Multiplexing) voltage sequence of 1000 samples, sampled

at 400 kHz, and of peak amplitude 9 V, is applied to one of the three TX coils using the FPGA analog outputs. This allows for a 400 Hz update rate.

- 2) The voltage time series induced in all three RX coils are recorded sequentially (in order to avoid crosstalk between coils) at a sampling rate of 400 kHz using the FPGA analog inputs.
- 3) A discrete Fourier transform is performed on the recorded time series, and for each one of them the magnitude of the component at 125 kHz is extracted, together with the corresponding sign which is obtained from the phase spectrum.
- 4) Steps 1-3 are repeated three times in total, one time for each TX coil, thus obtaining 9 magnitudes in total.
- 5) The  $3 \times 3$  channel matrix  $\mathbf{S}$  is assembled for one RX ground truth position. This concludes a measurement at a single  $x, y, z$  position.
- 6) The linear slides move the RX to a new  $x, y, z$  ground truth position, and the above procedure is repeated for the entire measurement grid.
- 7) RX positions w.r.t TX are extracted by optimizing against the modeled magnetic field of the TX.

A block diagram of the experiment can be seen in Fig. 3.

##### B. Channel Sounding

In order to estimate channel characteristics, we transmitted a periodic OFDM sequence, which was pre-programmed into the block memory of the FPGA module. The Fourier transform of both the received voltage  $Y_i(t)$  and the transmitted



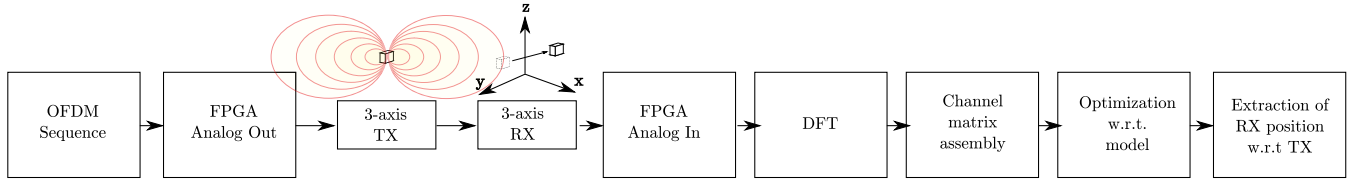


Fig. 3. Block diagram of the experimental setup.

voltage  $X_j(t)$  is taken, in order to then compute the transfer function  $S_{ij}(\omega) = Y_i(\omega)/X_j(\omega)$  corresponding to the channel between the  $i$ th RX coil and  $j$ th TX coil. In order to assemble the channel matrix  $\mathbf{S}$ , we extracted the amplitude of the coil self-resonant frequency (125 kHz) from the magnitude spectrum  $|S_{ij}(\omega)|$  and the sign from phase spectrum  $\arg(S_{ij}(\omega))$ , for all 9 Fourier spectra  $S_{ij}(\omega)$ . This procedure was repeated 1000 times, once for each 3-D position within the 30 mm  $\times$  30 mm  $\times$  30 mm cube, in order to construct the family of matrices  $\mathbf{S}^{k,l,m}$ , where  $k, l$  and  $m$  correspond to the indices of the  $x, y$  and  $z$  positions respectively.

### C. Channel Calibration

Before attempting to obtain a position estimate from measurements of the magnetic field, it is necessary to calibrate these measurements with respect to the model of (2). This is possible by formulating a cost function subject to the following constraints:

$$\{\hat{\mathbf{t}}, \hat{\mathbf{K}}\} = \arg \min_{\mathbf{t}, \mathbf{K}} \sum_{k,l,m} \|\mathbf{K} \odot \mathbf{S}_{\text{meas}}^{k,l,m}(\mathbf{t}) - \mathbf{S}_{\text{model}}^{k,l,m}(\mathbf{t})\|_F \quad (5)$$

where  $\mathbf{t} = [x_t, y_t, z_t]^T$  is the position vector between the world origin and TX (refer to Fig. 9). The input to the calibration algorithm is the vector  $\mathbf{p}$ , which is our ground truth position in the world frame (the world origin is defined with respect to the linear positioning stage), such that  $\mathbf{p} = \mathbf{t} + \mathbf{r}$ .  $\mathbf{K}$  is a calibration matrix,  $\odot$  denotes the Hadamard product of two matrices,  $\|\cdot\|_F$  denotes the Frobenius norm,  $\mathbf{S}_{\text{meas}} = c_{\text{meas}} \mathbf{B}_{\text{meas}}$  and  $\mathbf{S}_{\text{model}} = c_{\text{model}} \mathbf{B}_{\text{model}}$  (assuming that for now  $\mathbf{\Omega}_{\text{VW}}^T = \mathbf{I}$ ).

To avoid overfitting, and to obtain separate calibration coefficients for each coil on RX and TX, after  $\mathbf{K}$  is found, it is decomposed into the outer product of two vectors  $\mathbf{k}_{\text{RX}}$  and  $\mathbf{k}_{\text{TX}}$ , containing the calibration coefficients for RX and TX respectively. Motivated by the fact that

$$\mathbf{K} \odot \mathbf{S}_{\text{meas}} = \sigma_{\text{max}} \mathbf{K}_{\text{RX}} \mathbf{S}_{\text{meas}} \mathbf{K}_{\text{TX}} \quad (6)$$

where  $\mathbf{K}_{\text{RX}} = \text{diag}(\mathbf{k}_{\text{RX}})$  and  $\mathbf{K}_{\text{TX}} = \text{diag}(\mathbf{k}_{\text{TX}})$  are diagonal,  $\mathbf{K}$  was decomposed using singular value decomposition, to produce

$$\mathbf{K} = \mathbf{U} \mathbf{\Sigma} \mathbf{V} = \sum_{i=1}^M \sigma_i \mathbf{u}_i \mathbf{v}_i^T \quad (7)$$

The new calibration matrix  $\mathbf{K}_{\text{new}} = \sigma_{\text{max}} \mathbf{k}_{\text{RX}} \mathbf{k}_{\text{TX}}^T$ , where  $\sigma_{\text{max}}$  is the maximum singular value, and  $\mathbf{k}_{\text{RX}}$  and  $\mathbf{k}_{\text{TX}}$  are the corresponding left and right singular vectors respectively. It was found that the maximum singular value was two orders of magnitude greater than the others, which ensures that the

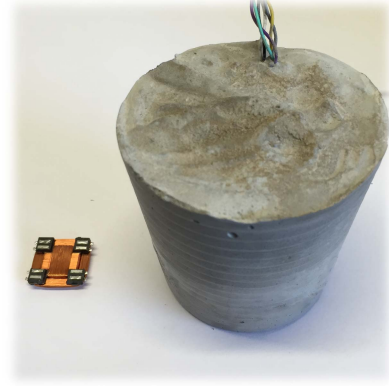


Fig. 4. Example transceiver coil, shown in air (left) and embedded within concrete (right).

coils are orthogonal. Furthermore,  $\|\mathbf{k}_{\text{RX}} \mathbf{k}_{\text{TX}}^T\| = 1$ , which implies that  $\sigma_{\text{max}} = c_{\text{model}}/c_{\text{meas}}$  is the proportionality constant between model and measurement.

### D. Position Estimation in 3-D

It is possible to obtain an estimate of RX position  $\mathbf{r}$  with respect to TX by formulating a cost function subject to the following constraints:

$$\hat{\mathbf{r}} = \arg \min_{\mathbf{r}} \|\sigma_{\text{max}} \mathbf{K}_{\text{RX}} \mathbf{S}_{\text{meas}}(\mathbf{r}) \mathbf{K}_{\text{TX}} - \mathbf{S}_{\text{model}}(\mathbf{r})\|_F \quad (8)$$

## V. EXPERIMENTAL RESULTS

The results of estimating absolute position using (8) are shown in Figs. 5 and 6. It is evident from the magnetic field plots (Fig. 2), as well as the cumulative error plots and histograms of the errors (Fig. 5) that the rectangular coil model, which accounts for the finite dimensions of the coils in the TX node, outperforms the infinitesimal dipole model. This statement is also supported by the fact that the errors are normally distributed. From the cumulative distributions of the errors, it was possible to calculate a median accuracy of 0.5 mm. Fig. 6 shows the actual position vs. estimated position for the rectangular coil model, for all  $x, y$  and  $z$  directions. Regarding the issue of linearity, it should be noted that even though the magnetic channel model of (2) is non-linear, owing to the  $r^3$  term in the denominator, the 3-D optimization algorithm outputs a position vector estimate by default, essentially linearizing the input-output relationship (Fig. 6), which is why we also quoted accuracy instead of linearity in Table I.

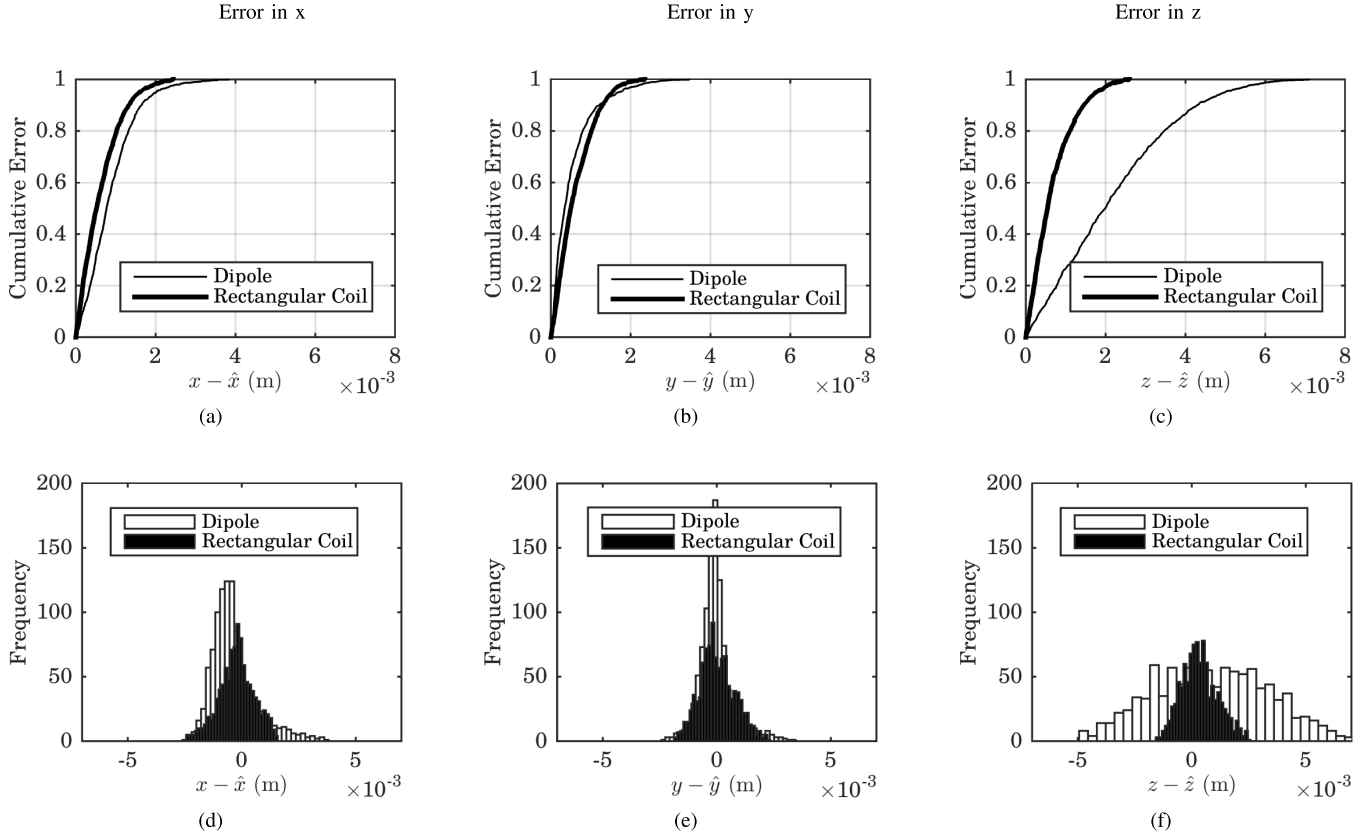


Fig. 5. Representation of cumulative error in (a) x-axis, (b) y-axis, (c) z-axis, and histogram of errors in (d) x-axis, (e) y-axis, (f) z-axis, for the dipole and rectangular coil models. The median error calculated from the rectangular coil model curves in (a)-(c) is 0.5 mm.

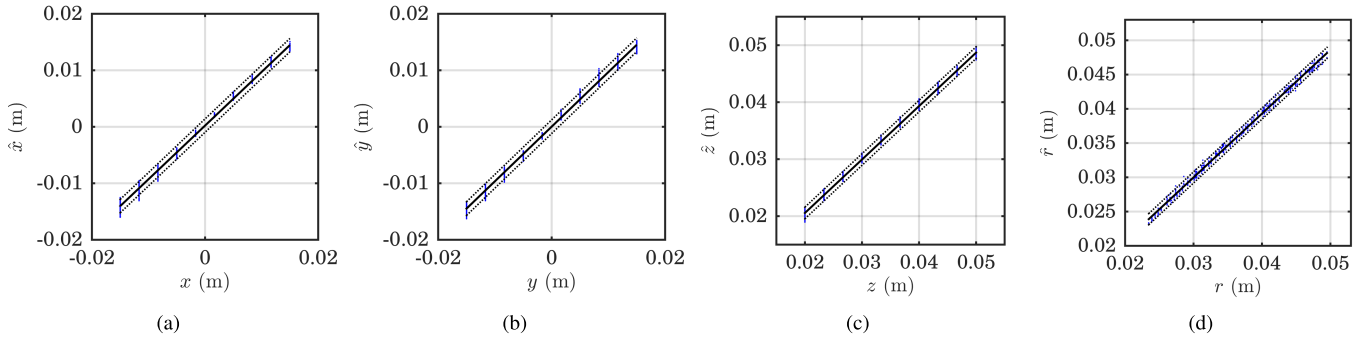


Fig. 6. Actual position vs. estimated position for the rectangular coil model, for all (a)  $x$ , (b)  $y$  and (c)  $z$  directions, as well as the magnitude  $r$  of the position vector  $\mathbf{r}$  (d).

There are a number of parameters that can be quoted when characterizing sensors (range, resolution, accuracy, linearity, sensitivity, sensing frequency, reliability, drift, size, cost) [59], [60] and their definitions and assigned importance vary slightly among manufacturers, researchers, and specific application requirements. To characterize our device as a displacement sensor, we are able to quote the range, resolution, and accuracy, as well as the system's spatial degrees of freedom, which is one of its unique features.

#### A. Range

Range is the minimum to maximum distance for which the sensor is able to produce a predictable output. This quantity is determined partially by the signal-to-noise ratio, channel

model accuracy, as well as by the calibration algorithm. Due to physical setup constraints (maximum travel distance of displacement stage) and model limitations, we chose  $-15 < x < 15$ ,  $-15 < y < 15$ ,  $20 < z < 50$  (mm) as calibration range.

#### B. Resolution

The root mean square (R.M.S.) error  $\text{err}_{\text{RMS}}$  for a particular value of  $r$  is defined as

$$\text{err}_{\text{RMS}}(r) = \sqrt{\frac{1}{N} \sum_i (\hat{r}_i - r)^2}, \quad (9)$$

where  $\hat{r}_i$  are the measurements (estimated distances) corresponding to a particular ground truth value  $r$ , with  $1 \leq i \leq N$ . Resolution is the minimum possible change in measured

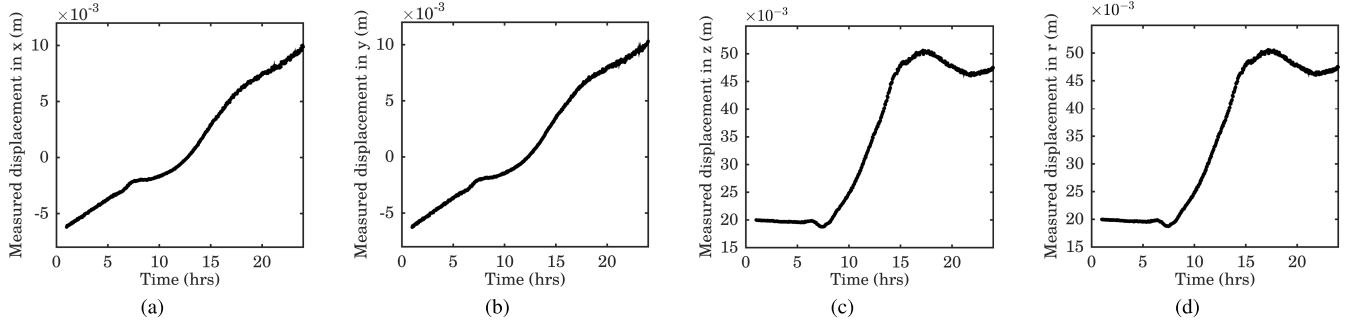


Fig. 7. Monitoring of gap widening in expansion joint due to temperature variation over the course of a day. The positioning stage was set up to follow a trajectory that simulates that of an expansion joint on a bridge deck. The receiver was able to very accurately estimate the ground truth trajectory, such that the two curves are overlaid. Figures correspond to the (a)  $x$ , (b)  $y$  and (c)  $z$  directions, as well as the magnitude  $r$  of the position vector  $r$  (d).

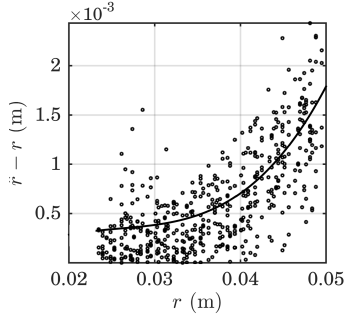


Fig. 8. Errors  $\hat{r} - r$  vs. ground truth position  $r$ , along with a trendline fitted to the root mean squares of the errors. From this figure we can derive a resolution of 0.5%, and an accuracy of 3.5%.

displacement that can be measured given a change in ground truth displacement, thus

$$\text{Resolution} = \min(\text{err}_{\text{RMS}}(r)) \quad (10)$$

In deriving figures for root mean square resolution and accuracy, the overall positioning error  $\hat{r} - r$  was plotted versus ground truth distance  $r$  (Fig. 8). The root mean square of the errors for each unique  $r$  was calculated according to (9), giving a resolution of  $\sim 250\mu\text{m}$ , or equivalently 0.5% w.r.t. full-scale output, given a maximum ground truth distance  $r_{\text{max}}$  of 5 cm.

### C. Accuracy

Accuracy is the maximum difference between measured displacement and ground truth displacement, thus

$$\text{Accuracy} = \max(\text{err}_{\text{RMS}}(r)) \quad (11)$$

Calculating from Fig. 8 it is 3.5%, w.r.t. full-scale output.

### D. Case Study

To evaluate our sensor in the context of a realistic displacement trajectory, we programmed the positioning stage to follow a trajectory similar to that caused by a temperature-induced expansion in a bridge. The results (Fig. 7) demonstrate that the sensor can easily track displacements within the volume quoted in Section V-A.

## VI. CHALLENGES AND LIMITATIONS

Having conducted the proof of concept in a noise-proof laboratory setting, we cannot as of yet guarantee the aforementioned positioning accuracy at all times, especially in electrically and magnetically noisy environments, such as rail environments, where harmonic fields due to the passage of rolling stock and pantograph-catenary arcing may disturb sensor operation. Studies on electromagnetic noise emerging within, without, and in the vicinity of rolling stock [61], [62] make reference to a number of noise sources: inductive noise sources, which include the mutual magnetic coupling between parallel electric traction, power and telecommunications lines, loop coupling between traction and signalling circuits, as well as coupling from vehicle power systems; radiative coupling sources, which can occur due to pantograph-catenary arcing and fast current switching in converters. Predicting electromagnetic noise emissions using computer simulations is currently not possible. Any attempt to replicate electromagnetic noise in the laboratory will yield inaccurate results, as the factors that affect noise in real deployment environments are extensive.

Another point worth mentioning is the sensitivity of the sensor to nearby conducting objects. In response to a primary alternating magnetic field, circulating currents form in conducting objects, producing secondary magnetic fields which combine with the primary fields. As a result, the received magnetic field distribution is distorted, which would in turn lead to a decrease in positioning accuracy. By modifying the physical model of the magnetic field to include metallic objects of certain geometries [40], [43], one can reduce this effect, as long as the metallic object is not situated between the sensor pair, such that the magnetic field of the transmitter is completely obstructed. Another way to account for the metallic objects is via statistical learning algorithms, in case the prior geometric configuration is unknown.

## VII. CONCLUSIONS AND FUTURE DIRECTIONS

In this work, we demonstrate proof of concept of a novel 3-D displacement measurement system that makes use of low frequency magnetic fields. Due to the fact that dielectric media such as concrete, water and soil are transparent to low frequency magnetic fields, the proposed system is ideal for



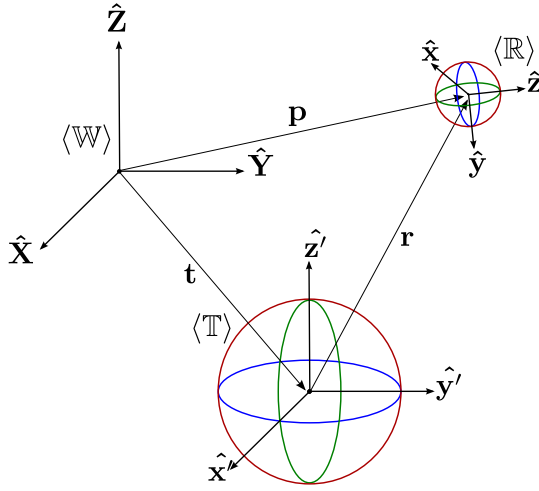


Fig. 9. World ( $\langle W \rangle$ ), transmitter ( $\langle T \rangle$ ) and receiver ( $\langle R \rangle$ ) frames. In this work, we position the transmitter at the origin of the world coordinate frame, which gives  $\mathbf{t} = \mathbf{0}$  and thus  $\mathbf{p} = \mathbf{r} = [x, y, z]^T$ .

embedding within concrete structures. This can be used for precise alignment of pre-manufactured parts during construction and also for monitoring the width of the gap between expansion joints. The transceivers were calibrated for a range of  $-15$  to  $15$  mm in the  $x$  and  $y$  directions and  $20$  to  $50$  mm in the  $z$  direction, and achieve a median positioning error of  $0.5$  mm in all directions. Resolution and accuracy with respect to full scale output were calculated as  $0.5\%$  and  $3.5\%$ , respectively, while the maximum update rate is  $400$  Hz. The sensor can be used for the structural health monitoring of civil structures, such as roads, railroads and bridges, helping to warn of impending failure and informing repair operations for improving safety conditions. Future work will include miniaturization of the sensors, as well as field trials.

#### APPENDIX DEFINITIONS OF REFERENCE FRAMES

Figure (9) depicts the system of two triaxial units, placed in the world frame ( $\langle W \rangle$ ), with each one having their own frames, ( $\langle T \rangle$ ) and ( $\langle R \rangle$ ). The transmitter and receiver orientations can be related by the following equations:

$$\text{TX position}|_{\langle W \rangle} = \mathbf{t} \quad (12)$$

$$\text{TX orientation}|_{\langle W \rangle} = \Theta|_{\langle W \rangle} \quad (13)$$

$$\text{RX position}|_{\langle T \rangle} = \mathbf{r} \quad (14)$$

$$\text{RX orientation}|_{\langle T \rangle} = \Omega|_{\langle T \rangle} \quad (15)$$

$$\text{RX position}|_{\langle W \rangle} = \mathbf{p} = \mathbf{t}|_{\langle W \rangle} + \Theta|_{\langle W \rangle} \mathbf{r} \quad (16)$$

$$\text{RX orientation}|_{\langle W \rangle} = \Omega|_{\langle W \rangle} = \Theta|_{\langle W \rangle} \Omega|_{\langle T \rangle} \quad (17)$$

In summary,  $\Theta|_{\langle W \rangle}$ ,  $\Omega|_{\langle T \rangle}$  and  $\Omega|_{\langle W \rangle}$  are rotation matrices, where  $\Theta|_{\langle W \rangle}$  rotates from TX to world coordinates,  $\Omega|_{\langle T \rangle}$  rotates from RX to TX coordinates, and  $\Omega|_{\langle W \rangle}$  rotates from RX to world coordinates. For the present paper, we have set  $\Theta|_{\langle W \rangle} = \Omega|_{\langle W \rangle} = \mathbf{I}$ .

#### ACKNOWLEDGMENT

The authors would like to thank EPSRC for funding this research (Grant ref. EP/M017583/1 Magneto-Inductive Six Degree of Freedom Smart Sensors (MiSixthSense) for Structural and Ground Health Monitoring).

#### REFERENCES

- [1] P. C. Chang, A. Flatau, and S. C. Liu, "Review paper: Health monitoring of civil infrastructure," *Struct. Health Monit.*, vol. 2, no. 3, pp. 257–267, 2003.
- [2] J. P. Lynch and K. J. Loh, "A summary review of wireless sensors and sensor networks for structural health monitoring," *Shock Vibrat. Dig.*, vol. 38, no. 2, pp. 91–130, 2006.
- [3] H. Yu and D. Jeong, "Railroad tie responses to directly applied rail seat loading in ballasted tracks: A computational study," in *Proc. Joint Rail Conf. Amer. Soc. Mech. Eng.*, 2012, pp. 123–132.
- [4] S. Kaewunruen and A. M. Remennikov, "Progressive failure of pre-stressed concrete sleepers under multiple high-intensity impact loads," *Eng. Struct.*, vol. 31, no. 10, pp. 2460–2473, Oct. 2009.
- [5] S. Kaewunruen and A. M. Remennikov, "Dynamic crack propagations in prestressed concrete sleepers in railway track systems subjected to severe impact loads," *J. Struct. Eng.*, vol. 136, no. 6, pp. 749–754, 2009.
- [6] A. P. Adewuyi, Z. Wu, and N. H. M. K. Serker, "Assessment of vibration-based damage identification methods using displacement and distributed strain measurements," *Struct. Health Monit.*, vol. 8, no. 6, pp. 443–461, Nov. 2009.
- [7] Y. Ni, X. Hua, K. Wong, and J. Ko, "Assessment of bridge expansion joints using long-term displacement and temperature measurement," *J. Perform. Construct. Facilities*, vol. 21, no. 2, pp. 143–151, 2007.
- [8] S. Moorthy and C. W. Roeder, "Temperature-dependent bridge movements," *J. Struct. Eng.*, vol. 118, no. 4, pp. 1090–1105, 1992.
- [9] K.-T. Park, S.-H. Kim, H.-S. Park, and K.-W. Lee, "The determination of bridge displacement using measured acceleration," *Eng. Struct.*, vol. 27, no. 3, pp. 371–378, Feb. 2005.
- [10] J.-W. Park, S.-H. Sim, H.-J. Jung, and B. F. Spencer, Jr., "Development of a wireless displacement measurement system using acceleration responses," *Sensors*, vol. 13, no. 7, pp. 8377–8392, 2013.
- [11] H. Sekiya, K. Kimura, and C. Miki, "Technique for determining bridge displacement response using MEMS accelerometers," *Sensors*, vol. 16, no. 2, p. 257, 2016.
- [12] X. Zhao *et al.*, "Bridge displacement monitoring method based on laser projection-sensing technology," *Sensors*, vol. 15, no. 4, pp. 8444–8463, 2015.
- [13] J. J. Lee and M. Shinozuka, "A vision-based system for remote sensing of bridge displacement," *Ndt & E Int.*, vol. 39, no. 5, pp. 425–431, Jul. 2006.
- [14] D. Lecomte, J. Vantomme, and H. Sol, "Crack detection in a concrete beam using two different camera techniques," *Struct. Health Monit.*, vol. 5, no. 1, pp. 59–68, 2006.
- [15] Z. Yin, C. Wu, and G. Chen, "Concrete crack detection through full-field displacement and curvature measurements by visual mark tracking: A proof-of-concept study," *Struct. Health Monit.*, vol. 13, no. 2, pp. 205–218, 2014.
- [16] H. S. Park, H. M. Lee, H. Adeli, and I. Lee, "A new approach for health monitoring of structures: Terrestrial laser scanning," *Comput.-Aided Civil Infrastruct. Eng.*, vol. 22, no. 1, pp. 19–30, Jan. 2007.
- [17] S. W. Park, H. S. Park, J. H. Kim, and H. Adeli, "3D displacement measurement model for health monitoring of structures using a motion capture system," *Meas.*, vol. 59, pp. 352–362, Jan. 2014.
- [18] H. Jo, S.-H. Sim, A. Tatkowski, B. F. Spencer, Jr., and M. E. Nelson, "Feasibility of displacement monitoring using low-cost gps receivers," *Struct. Control Health Monit.*, vol. 20, no. 9, pp. 1240–1254, Sep. 2013.
- [19] S. Vurpillot, N. Casanova, D. Inaudi, and P. Kronenberg, "Bridge spatial displacement monitoring with 100 fiber optic deformation sensors: Sensors network and preliminary results," in *Proc. SPIE*, vol. 51, pp. 51–57, May 1997.
- [20] C. Rodrigues, C. Félix, and J. Figueiras, "Fiber-optic-based displacement transducer to measure bridge deflections," *Struct. Health Monit.*, vol. 10, no. 2, pp. 147–156, 2011.
- [21] N. Metje, D. N. Chapman, C. D. F. Rogers, P. Henderson, and M. Beth, "An optical fiber sensor system for remote displacement monitoring of structures—Prototype tests in the laboratory," *Struct. Health Monit.*, vol. 7, no. 1, pp. 51–63, 2008.

- [22] Mageba S.A., Bülach, Switzerland. (2016). *RoboSMART*. [Online]. Available: <http://www.mageba.ch/>
- [23] H. Adeli, W. Weaver, and J. Gere, "Algorithms for nonlinear structural dynamics," *J. Struct. Division*, vol. 104, no. 2, pp. 263–280, 1978.
- [24] A. Markham, N. Trigoni, D. W. Macdonald, and S. A. Ellwood, "Underground localization in 3-D using magneto-inductive tracking," *IEEE Sensors J.*, vol. 12, no. 6, pp. 1809–1816, Jun. 2012.
- [25] A. Plotkin, O. Shaffir, E. Paperno, and D. M. Kaplan, "Magnetic eye tracking: A new approach employing a planar transmitter," *IEEE Trans. Biomed. Eng.*, vol. 57, no. 5, pp. 1209–1215, May 2010.
- [26] J. S. Day, D. J. Murdoch, and G. A. Dumas, "Calibration of position and angular data from a magnetic tracking device," *J. Biomech.*, vol. 33, no. 8, pp. 1039–1045, Aug. 2000.
- [27] B. E. Fischer, I. J. LaHaie, D. D. Arumugam, J. D. Griffin, D. D. Stancil, and D. S. Ricketts, "Three-dimensional position and orientation measurements using magneto-quasistatic fields and complex image theory," *IEEE Antennas Propag. Mag.*, vol. 56, no. 1, pp. 160–173, Feb. 2014.
- [28] L.-M. Chang and Y.-J. Lee, "Evaluation of performance of bridge deck expansion joints," *J. Perform. Construct. Facilities*, vol. 16, no. 1, pp. 3–9, 2002.
- [29] Division of Maintenance Pavement Program, "Concrete pavement guide part 3: Preservation strategies chapter 360—Joint and crack sealing," Dept. Transp., Tech. Rep., 2015. [Online]. Available: [http://www.dot.ca.gov/hq/maint/Pavement/Offices/Pavement\\_Engineering/CPG/CPG\\_Ch360\\_Joint\\_Seal.pdf](http://www.dot.ca.gov/hq/maint/Pavement/Offices/Pavement_Engineering/CPG/CPG_Ch360_Joint_Seal.pdf)
- [30] S. Fericean and R. Droxler, "New noncontacting inductive analog proximity and inductive linear displacement sensors for industrial automation," *IEEE Sensors J.*, vol. 7, no. 11, pp. 1538–1545, Nov. 2007.
- [31] R. Bhattacharyya, P. Kalansuriya, and S. Sarma, "An antenna-based RFID expansion joint monitor," in *Proc. IEEE Antennas Propag. Soc. Int. Symp. (APSURSI)*, Jul. 2013, pp. 2305–2306.
- [32] C. Mandel, B. Kubina, M. Schüller, and R. Jakoby, "Passive chipless wireless sensor for two-dimensional displacement measurement," in *Proc. 41st Eur. Microw. Conf. (EuMC)*, Oct. 2011, pp. 79–82.
- [33] J. Siden, X. Zeng, T. Unander, A. Koptyug, and H.-E. Nilsson, "Remote moisture sensing utilizing ordinary RFID tags," in *Proc. IEEE Sensors*, Oct. 2007, pp. 308–311.
- [34] Messtechnik GmbH & Co. KG, Ortenburg, Germany. (2016). *Micro-Epsilon*. [Online]. Available: <http://www.micro-epsilon.com/>
- [35] Capacitec Inc., Ayer, MA, USA. (2016). [Online]. Available: <http://www.capacitec.com/>
- [36] Oakdale, MN, USA. (2016). *Lion Precision*. [Online]. Available: <http://www.lionprecision.com/>
- [37] Neuhausen, Germany. (2016). *Balluff GmbH*. [Online]. Available: <http://www.balluff.com/>
- [38] Keyence Corp., Osaka, Japan. (2016). [Online]. Available: <http://www.keyence.co.jp/>
- [39] R. Bhattacharyya, C. Floerkemeier, and S. Sarma, "Towards tag antenna based sensing—An RFID displacement sensor," in *Proc. IEEE Int. Conf. RFID*, Apr. 2009, pp. 95–102.
- [40] O. Kypris, T. E. Abrudan, and A. Markham, "Reducing magneto-inductive positioning errors in a metal-rich indoor environment," in *Proc. IEEE SENSORS*, Nov. 2015, pp. 1–4.
- [41] T. E. Abrudan, Z. Xiao, A. Markham, and N. Trigoni, "Underground incrementally deployed magneto-inductive 3-D positioning network," *IEEE Trans. Geosci. Remote Sens.*, vol. 54, no. 8, pp. 4376–4391, Aug. 2016.
- [42] F. H. Raab, E. B. Blood, T. O. Steiner, and H. R. Jones, "Magnetic position and orientation tracking system," *IEEE Trans. Aerosp. Electron. Syst.*, vol. AES-15, no. 5, pp. 709–718, Sep. 1979.
- [43] O. Kypris, T. E. Abrudan, and A. Markham, "Magnetic induction-based positioning in distorted environments," *IEEE Trans. Geosci. Remote Sens.*, vol. 54, no. 8, pp. 4605–4612, Aug. 2016.
- [44] J. I. Agbinya, *Principles of Inductive Near Field Communications for Internet of Things* (River Publishers Series on Communications). Aalborg, Denmark: River Publishers, 2011.
- [45] J. B. Kuipers, *Quaternions and Rotation Sequences. A Primer With Applications to Orbits, Aerospace, and Virtual Reality*. Princeton, NJ, USA: Princeton Univ. Press, 1999.
- [46] A. Markham and N. Trigoni, "Magneto-inductive networked rescue system (MINERS): Taking sensor networks underground," in *Proc. 11th Int. Conf. Inf. Process. Sensor Netw. (IPSN)*, Apr. 2012, pp. 317–328.
- [47] A. Markham, N. Trigoni, S. A. Ellwood, and D. W. Macdonald, "Revealing the hidden lives of underground animals using magneto-inductive tracking," in *Proc. 8th ACM Conf. Embedded Netw. Sensor Syst.*, Nov. 2010, pp. 281–294.
- [48] M. Agrawal and K. Konolige, "Real-time localization in outdoor environments using stereo vision and inexpensive GPS," in *Proc. 18th Int. Conf. Pattern Recognit. (ICPR)*, vol. 3, Aug. 2006, pp. 1063–1068.
- [49] G. Pirkel and P. Lukowicz, "Robust, low cost indoor positioning using magnetic resonant coupling," in *Proc. ACM Conf. Ubiquitous Comput.*, Sep. 2012, pp. 431–440.
- [50] X. Tan, Z. Sun, and P. Wang, "On localization for magnetic induction-based wireless sensor networks in pipeline environments," in *Proc. IEEE Int. Conf. Commun. (ICC)*, Jun. 2015, pp. 2780–2785.
- [51] A. Sheinker, B. Ginzburg, N. Salomonski, L. Frumkis, and B.-Z. Kaplan, "Localization in 3-D using beacons of low frequency magnetic field," *IEEE Trans. Instrum. Meas.*, vol. 62, no. 12, pp. 3194–3201, Dec. 2013.
- [52] R. P. Feynman, R. B. Leighton, and M. Sands, *The Feynman Lectures on Physics*, vol. 2. Reading, MA, USA: Addison Wesley, 1964.
- [53] T. E. Abrudan, Z. Xiao, A. Markham, and N. Trigoni, "Distortion rejecting magneto-inductive three-dimensional localization (MagLoc)," *IEEE J. Sel. Areas Commun.*, vol. 33, no. 11, pp. 2404–2417, Nov. 2015.
- [54] M. Misakian, "Equations for the magnetic field produced by one or more rectangular loops of wire in the same plane," *J. Res. Nat. Inst. Standards Technol.*, vol. 105, no. 4, p. 557, 2000.
- [55] Campanillas, Malaga, Spain. (2016). *PREMO Group*. [Online]. Available: <http://www.grupopremo.com/>
- [56] Zaber Technologies, Vancouver, BC, Canada. (2016). [Online]. Available: <https://www.zaber.com/>
- [57] Nat. Instrum. Corp., Austin, TX, USA. (2016). [Online]. Available: <http://www.ni.com/>
- [58] *MATLAB Version 8.5.0.197613 (R2015a)*, MathWorks Inc., Natick, MA, USA, 2015.
- [59] J. Shieh, J. E. Huber, N. A. Fleck, and M. F. Ashby, "The selection of sensors," *Prog. Mater. Sci.*, vol. 46, nos. 3–4, pp. 461–504, 2001.
- [60] J. J. Carr and J. M. Brown, *Introduction to Biomedical Equipment Technology*. Englewood Cliffs, NJ, USA: Prentice-Hall, 1993.
- [61] R. J. Hill, "Electric railway traction. VI. Electromagnetic compatibility disturbance-sources and equipment susceptibility," *Power Eng. J.*, vol. 11, no. 1, pp. 31–39, Feb. 1997.
- [62] D. Bellan, A. Gaggelli, F. Maradei, A. Mariscotti, and S. A. Pignari, "Time-domain measurement and spectral analysis of nonstationary low-frequency magnetic-field emissions on board of rolling stock," *IEEE Trans. Electromagn. Compat.*, vol. 46, no. 1, pp. 12–23, Feb. 2004.
- [63] K. Dospial. (2015). *Railway Tracks* [Online]. Available: <https://grabcad.com/library/railway-tracks-1>



**Orfeas Kypris** (S'11–M'15) received the B.Eng. degree in electrical and electronic engineering in 2009, and the M.Sc. degree in magnetics in 2010 from Cardiff University, Cardiff, U.K. He then joined the Department of Electrical and Computer Engineering at Iowa State University, USA, where he received the Ph.D. degree in electrical engineering in 2015. Since 2015, he has been a Postdoctoral Researcher with the Department of Computer Science, University of Oxford, working on indoor localization and structural health monitoring using low-frequency magnetic fields. His research interests include non-destructive evaluation using Barkhausen signals, applied electromagnetism and magnetic materials. He is a member of Eta Kappa Nu (IEEE HKN) and the IEEE Magnetics Society.



**Andrew Markham** received the bachelor's degree in 2004 and Ph.D. degree in 2008 in electrical engineering from the University of Cape Town, South Africa. He is currently an Associate Professor with the Department of Computer Science, University of Oxford, working with the Sensor Networks Group. His research interests include low-power sensing, embedded systems and magneto-inductive techniques for positioning and communication.